Land-surface, boundary layer and cloud-field coupling over the Amazon in ERA-40

Alan K. Betts[1] and Pedro Viterbo[2]

[1] *Atmospheric Research, Pittsford, Vermont*
[2] *ECMWF, Reading, England*
[1] Corresponding author address: *Alan K. Betts, Atmospheric Research, 58 Hendee Lane, Pittsford, VT 05763; e-mail: akbetts@aol.com*

Abstract

Models are a powerful tool for understanding the coupling of physical processes. We illustrate this using ERA-40 data for the Madeira river, a south-western basin of the Amazon, which has a large seasonal cycle with a dry season in the austral winter. Daily averaged data, derived from basin-averaged hourly data, give a powerful description of this coupling of physical processes at the land-surface. The links that are visible on a daily timescale can also be seen on the seasonal timescale. Several important surface processes are strongly influenced by soil moisture: relative humidity which gives the mixed sub-cloud layer depth, low cloud cover and the surface net long-wave flux. The link between soil moisture and equivalent potential temperature can therefore be clearly seen once the temperature dependence is filtered. Surface evaporation is controlled as much by the feedback of the cloud field on the surface radiation budget as by soil moisture. Above the surface the cloud field and precipitation is coupled to the large-scale dynamics, specifically the mid-tropospheric omega field. The shortwave cloud forcing of the atmosphere and the surface is given by the cloud field albedo at the top of the atmosphere to better than 1%. We have developed a powerful methodology for comparing the feedback processes in different models with each other and with data.

1. Introduction

The complex interactions between the land-surface, the boundary layer (BL) and the cloud fields are central to the climate over land, but they are not well understood. They are clearly different in different models (Koster at al., 2002, 2004; Lawrence and Slingo, 2004), and both surface and atmospheric controls are involved (Findell and Eltahir, 2003). Betts et al. (1996) discussed the coupling of soil moisture, the surface fluxes, the deepening of the mixed layer and the rise of daytime equivalent potential temperature and evaporation-precipitation feedback. Small and Kurc (2003) have noted that in semiarid environments, the surface outgoing and net longwave fluxes are tightly coupled to soil moisture through the surface temperature. Betts (2004) proposed using global model data from reanalyses to explore quantitatively the coupling between different processes, and he suggested a framework for both model diagnostics, and for evaluating different models against data. He showed, using river-basin averaged data from the European Centre for Medium-range Weather Forecasts (ECMWF) reanalysis (ERA-40: Uppala et al., 2004), that the daily averaged land-surface state can be used to map the transitions of a model's surface climate; and to quantify the links between the soil moisture, the surface heat fluxes, the mean cloud-base and the short-wave (SW) and long-wave (LW) radiation fields at the surface. In a theoretical study using an idealized equilibrium BL, Betts et al. (2004) showed how the daily averaged energy, water and carbon fluxes were dependent on the coupling to the BL cloud field. Betts et al (2005a) also used ERA-40 data archived for one grid-point to discuss the critical role of cloud albedo on the surface energy budget over the boreal forest. In this paper, we extend these ideas again using ERA-40 data for an Amazon sub-basin. We will explore not only the coupling between the surface and BL, but also the relationship of the total cloud field and radiative forcing to surface processes, and the links between the vertical motion field and clouds and precipitation. We believe this provides a powerful quantitative framework for evaluating the links between the diabatic physical processes in models. For more than a decade, cloud feedbacks have been regarded as the major source of uncertainty in climate models: the framework we present here provides a new tool for understanding, and for evaluating different models against data. The important message is that the SW and

LW cloud radiative feedbacks, which are linked to soil moisture and boundary layer processes as well as the large scale dynamics, are tightly coupled to the land-surface interaction. We are using ERA-40 as a test data set for these ideas, recognizing that our results depend on the physical parameterizations in that model. Three papers have already assessed the systematic biases in temperature and the surface energy and water budgets of ERA-40 for the Mississippi, Mackenzie and Amazon river basins (Betts et al., 2003a,b, 2005b), and for the last fifteen years, the model systematic biases are small on monthly timescales. However, ERA-40 does have a known error in the diurnal cycle of precipitation over Amazonia (Betts and Jakob, 2002a,b). Even though the daily mean precipitation is quite accurate, when compared with observations from the Large-scale Biosphere-Atmosphere Experiment (LBA), precipitation occurs too early in the diurnal cycle. Recent revisions to the convection scheme, subsequent to ERA-40, have improved the diurnal cycle (Bechtold et al., 2004). In this paper we take only the first step of exploring the interrelationship of processes in the model: the next step of using independent datasets to evaluate the relationships of the coupled system is left for future work. Then it will be possible to assess how well different models couple the many linked processes in the energy and water cycle.

ERA-40 was extended to cover the 45 years from September, 1967 to August, 2002, but we shall only use data from the recent period, 1990-2001. The analysis system includes the land-surface scheme described in Van den Hurk et al. (2000), and a 3-D variational assimilation system. The horizontal resolution of the spectral model is triangular truncation at T_L-159, and there are 60 levels in the vertical, including a well-resolved boundary layer and stratosphere. Documentation of the Integrated Forecast System (IFS), cycle 23r4, and a summary and discussion of the observations available at different times during the 45-year reanalysis can be found at http://www.ecmwf.int/research/era/. Surface energy and water budgets, near-surface and sub-surface variables and atmospheric variables, averaged over river basins, were computed and archived (Kållberg et al., 2004) during the analysis cycle at an hourly timescale. This preserves the full model time resolution for all the fluxes and gives an hourly sample of the model prognostic fields, including the omega field. We have computed daily means from the 24-h forecasts from the 00 UTC analysis cycle, and from these also monthly means. Our analysis will use daily means from ERA-40 for the Madeira river, a south-western basin of the Amazon, roughly 1.3 10^6 km^2 in area (see Betts et al., 2005b).

2. Coupling of physical processes in ERA-40

We will use the reanalysis data to quantify the many physical processes which determine the land-surface energy and water balance. Soil moisture controls resistance to evaporation in the model (over a dynamic range between the model permanent wilting point, PWP, and the field capacity, FC), so we shall use it to organize the data. We define a soil moisture index for both the first model soil layer, SMI:L1, which is 7cm deep, and for the first three layers, which together are 100cm deep, which we will loosely call 'root-zone' soil moisture, SMI:root (for some vegetation classes, the model has some small percent of roots in the fourth soil layer, Van den Hurk et al., 2000). These indices are scaled, so that 0<SMI<1 as PWP<soil moisture<FC. The sub-cloud layer is a balance between the surface fluxes and the convective fluxes at cloud-base modified by diabatic processes in the sub-cloud layer, such as the radiative flux divergence and the evaporation of falling precipitation. We shall use the mean lifting condensation level (LCL) in pressure coordinates, P_{LCL}, which is closely a measure of the low-level relative humidity (RH) as a second way of organizing data. Previous studies have shown that it is closely linked to soil moisture (Betts and Ball, 1995, 1998; Betts, 2004), or to the availability of water for evaporation (Betts et al., 1999).

The cloud fields modify the SW and LW radiative flux at the surface (the so-called cloud forcing), so we shall use them as a third tool to organize the data. One of the fundamental relationships in the earth's climate is the link between the surface evaporative processes, the cloud field and the impact of the cloud field on the radiation budget. Water is evaporated at the earth's surface, convected aloft to moisten the atmosphere and to

form clouds, which both precipitate, releasing latent heat and modify the SW and LW radiation budget, both at the top of the atmosphere (TOA) and at the surface (SRF), as well as the energy budget of the atmosphere itself. Quantifying these links satisfactorily has been a goal of the US Global Change Research Program for more than a decade (USGCRP,1995). Our framework here is model data, but we plan to use the same framework to evaluate processes in different models against real observations. The ERA-40 archive (Kållberg et al., 2004) contains 'clear-sky' fluxes computed without the model cloud field, as well as the radiation fluxes computed with the model (prognostic) cloud field. By difference, we compute cloud forcing (CF) terms as

$$\text{SWCF:TOA} = \text{SW:TOA} - \text{SW:TOA(clear)} \quad (1a)$$

$$\text{LWCF:TOA} = \text{LW:TOA} - \text{LW:TOA(clear)} \quad (1b)$$

$$\text{SWCF:SRF} = \text{SW:SRF} - \text{SW:SRF(clear)} \quad (1c)$$

$$\text{LWCF:SRF} = \text{LW:SRF} - \text{LW:SRF(clear)} \quad (1d)$$

The atmosphere (ATM) cloud radiative forcing are the differences

$$\text{SWCF:ATM} = \text{SWCF:TOA} - \text{SW:SRF} \quad (2a)$$

$$\text{LWCF:ATM} = \text{LWCF:TOA} - \text{LW:SRF} \quad (2b)$$

To remove the effect of changing solar zenith angle it is useful to define TOA and SRF *cloud albedos*, defined as

$$\text{ALB:TOA} = 1 - \text{SW:TOA}/\text{SW:TOA(clear)} \quad (3a)$$

$$\text{ALB:SRF} = 1 - \text{SW:SRF}/\text{SW:SRF(clear)} \quad (3b)$$

These cloud albedos, which are derived here from the model archive fields, will be used as a quantitative measure of the cloud field. Conceptually one may think of these as being 'observables', easily derived from satellite data, as in the well-known methods for deriving the surface radiation budget (Pinker et al., 2003). We will also use SW:SRF(clear) to scale the other terms in the surface energy budget (see Figure 5 later).

2.1. Annual cycle for Madeira river basin

Before analyzing the daily data, we shall show the mean annual cycle for the 12 years 1990-2001 for the Madeira river, because several of the critical links can be seen even in monthly averaged data. Figure 1 has four panels, all showing the mean annual cycle as a function of the first model layer soil moisture index, SMI:L1. The numbers indicate the month. Panel (a) (top left) shows the annual cycle of temperature, T (at the lowest model level in the atmosphere, about 10m above the surface), showing a minimum in June and a maximum in October; and mixing ratio, Q, showing a minimum in July and a maximum in December. The annual range of T is quite small, but that of Q is quite large between the dry season (June to September) and the rainy season (November to April). Panel (b) shows the mean relative humidity, RH, and the equivalent potential temperature, θ_E. We see that RH (which being a measure of sub-saturation is tightly linked to cloud-base height: see below) is tightly coupled to soil moisture (see Betts, 2004) and follows a single path increasing and decreasing with SMI between dry and wet seasons. Both Q and θ_E, which can be thought of as different functions of T and RH, have similar annual cycles, increasing to a maximum in the rainy season, when precipitation is largest. Panel (c) shows fractional low, high and total cloud cover (LCC, HCC, TCC). We see that LCC depends almost linearly on SMI:L1 between dry and wet seasons, while HCC and TCC must depend as well on other processes. Panel (d) shows the surface radiation budget. The annual cycle of SW_{net} has similar values in July, when solar zenith angle is higher and cloud cover is at a minimum; as in January, when solar zenith angle is smaller, but cloud cover is at its maximum. Maximum SW_{net} is reached in October, when cloud cover is still relatively low. In contrast, outgoing LW_{net} decreases almost linearly as

SMI increases, as the subcloud layer get shallower and cloud cover increases (panel (1c) and Figures 2 and 14(a) later). Net radiation R_{net} is given by the sum

$$R_{net} = SW_{net} + LW_{net} \quad (4)$$

The seasonal cycle of R_{net} has a maximum in October and a minimum in June, as does temperature.

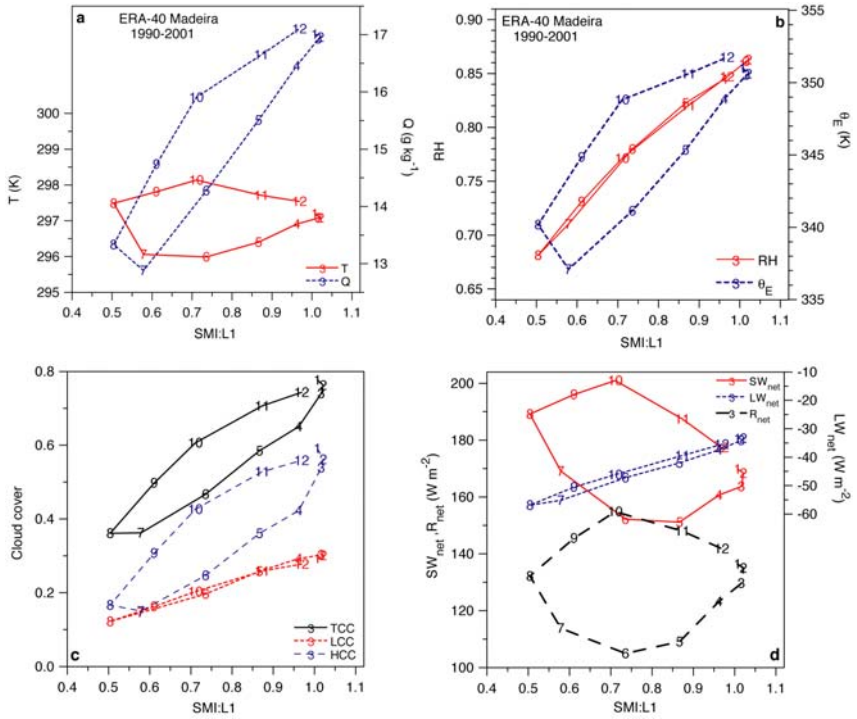

Figure 1: Mean annual cycle of a) Temperature and mixing ratio as a function of soil moisture index, SMI:L1, b) P_{LCL} and θ_E as a function of soil moisture index, c) LCC, HCC and TCC as a function of soil moisture index, d) SW_{net}, LW_{net}, R_{net} as a function of soil moisture index.

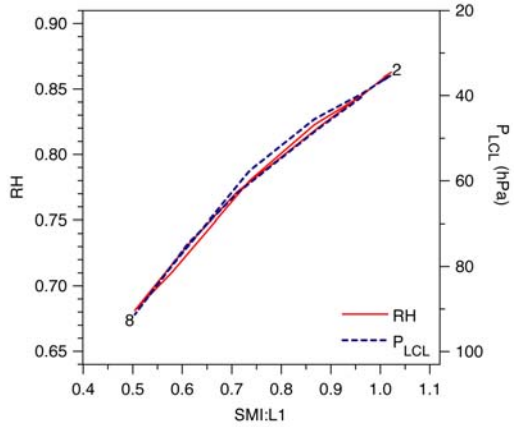

Figure 2: Annual cycle of RH and P_{LCL} as a function of soil moisture index, showing tight coupling.

Viewing the four panels as a whole we see that three distributions, RH, LCC and $LW_{net,}$ are represented by a single line, but the others are elliptical with a higher value in October than June. The higher October values of HCC and TCC are a consequence of a shift from basin-scale divergence in June to convergence in October (see Figure 3, later). Despite this, R_{net} is higher in October because of the smaller solar zenith angle, which gives a warmer mean temperature and a higher θ_E. We shall find that these tight links between SMI:L1, RH (and mean cloud-base, shown in Figure 2), LCC and LW_{net} are supported by the daily data as well. Above the boundary layer (BL), the large-scale dynamics are a controlling influence on the cloud cover on both the daily and seasonal timescales.

Figure 2 shows the tight relationship (Betts, 2003) between RH and the mean height of the lifting condensation level (in p-coordinates), P_{LCL}, which in the moist tropics can be considered the mean cloud-base (pressure) height. From August to February, RH and P_{LCL} follow one path with increasing SMI. In fact, low level RH, a measure of sub-saturation, and cloud-base height are essentially interchangeable in the mixed layer over land on all time-scales from the diurnal to the seasonal. The resistance to evaporation, which depends on soil moisture, leads to a drop in saturation across the leaf, which lowers RH and raises mean cloud-base. This is an important aspect of the coupling between soil moisture, plant processes, the BL and the cloud field, which is also linked back to the LW radiation budget at the surface, shown in Figure 1(d).

Figure 3 (a) shows the seasonal relationship between total column water vapor (TCWV, the 'precipitable water') and TCC and the SRF and TOA cloud albedos. The similarity between the patterns of TCC and the cloud albedos supports our use of the cloud albedos as a quantitative measure of cloud. The ratio of ALB:TOA/ALB:SRF is the line shown, which decreases from 0.77 to 0.74 as TCWV increases. This means that the TOA and SRF cloud albedos have a very tight relationship. We shall see that this is also true with daily data. Panel (3b) shows the annual cycle of TCWV, TCC and ALB:SRF as functions of the analysis mean vertically integrated moisture convergence, VIMC (an average from the four daily analysis times). The convergence of moisture into the basin increases TCWV and cloud cover, but it is not the sole control. Cloud albedo is higher in say May than September, because LCC, which is linked to SMI:L1, is higher (Figure 1c). Panel (3c) shows that precipitation, P, increases much more steeply with TCWV than evaporation, E. The difference, P-E, which panel (3d) shows is closely related to basin-scale atmospheric moisture convergence, changes sign in May and September between the dry and rainy seasons. The annual cycle of E is weak, with a minimum in June and July, when SMI and R_{net} are at a minimum, and a maximum in November and

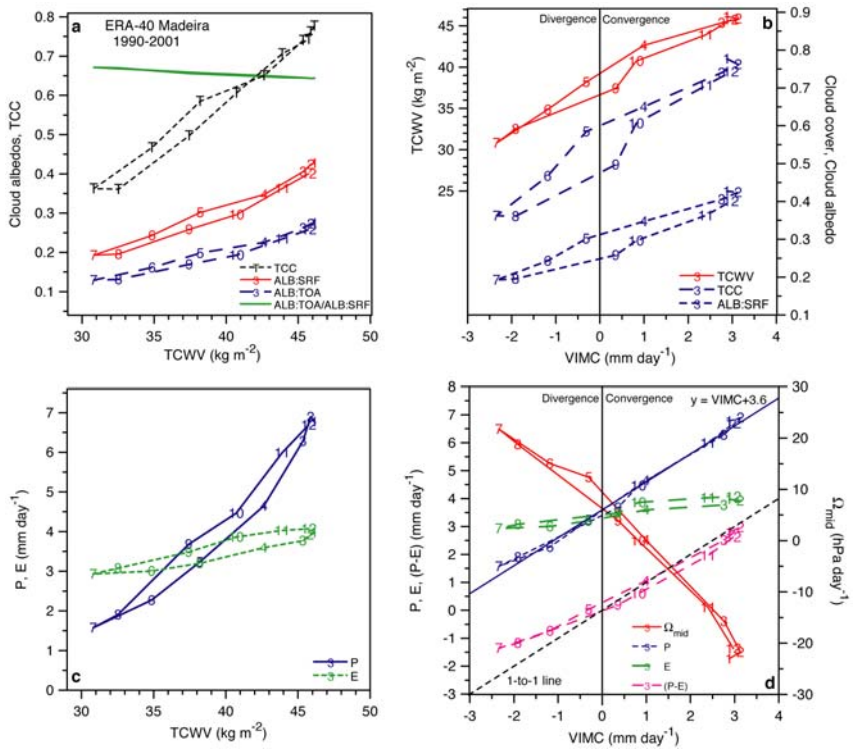

Figure 3: Mean annual cycle of a) TCC and cloud albedos as a function of TCWV, b) TCWV, TCC and surface cloud albedo as a function of VIMC, c) Precipitation and evaporation as a function of TCWV, d) P, E, (P-E) and Ω_{mid} as a function of VIMC.

December at the beginning of the rainy season. The stronger annual cycle of P clearly bears an important relationship to the annual cycle of TCWV (see also Betts et al (2005b). Panel (3d) shows the important dynamical links in the system. Over the annual cycle, the analysis VIMC is linked to P and (P-E) and to the monthly averaged mid-tropospheric omega field, Ω_{mid}. This was averaged from the hourly data and then over model levels in the middle troposphere, corresponding roughly to the layer between 300 and 700 hPa. Moisture divergence and mean subsidence are a maximum in July, and P is a minimum, while from December to February, convergence, mean ascent and precipitation reach their maximum in the rainy season. The line VIMC+3.6 shows that P is essentially determined by moisture convergence and mean evaporation (3.6 mm day^{-1}) on a monthly timescale. The divergence of (P-E) from the 1-to-1 line in the dry season means that the local change term, the mean drying of the atmosphere, is of order 1mm day^{-1}.

Figure 4 shows that the seasonal link between θ_E and P, though non-linear, is quite strong. Precipitation increases quite steeply once θ_E increases above 347K, a typical value for the equilibrium over the tropical oceans (Betts and Ridgway, 1989). However soil moisture for both the first layer and the root zone lags P, so that in the seasonal transitions of May and September, P is similar but the soil moisture is much drier in September.

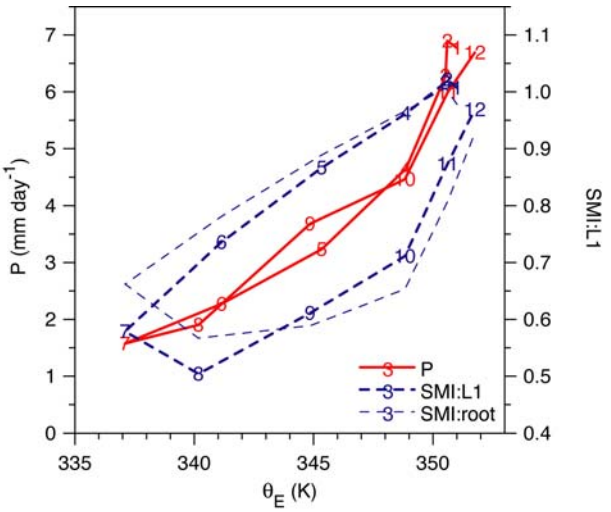

Figure 4: P and soil moisture indices as a function of θ_E.

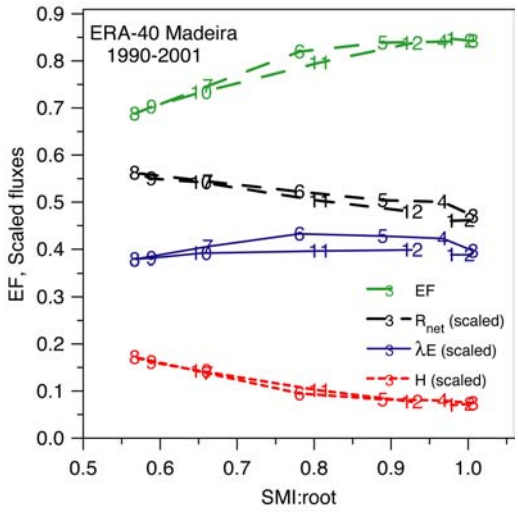

Figure 5: EF and scaled fluxes as a function of root zone SMI.

The annual cycle of the surface forcing of the rainy season circulation over the SW Amazon can be understood as follows. R_{net} is a minimum in June, when the solar elevation is lowest, and the basin temperature is the lowest. Basin soil moisture, RH and θ_E are both low. The circulation over the basin is divergent, P < E and SMI continues to fall and with it RH, θ_E and low cloud cover also fall, reaching a minimum in August. As the months progress and the sun returns south of the equator (towards near zenith at noon in December), R_{net} increases, warming the surface and increasing θ_E and precipitation heating of the atmosphere, and the mean circulation shifts from divergence to convergence by September. Precipitation increases soil moisture, and the rise of RH increases θ_E. Cloud cover increases also and after October is sufficient to reduce R_{net} even in the face of the higher solar elevation. However the rise of soil moisture, because P >E, keeps RH and θ_E at peak values from December to March, maintaining the rainy season precipitation and the latent heating driving the convergent circulation. But by April the continuing drop of incoming solar radiation, and fall of surface temperature in some sense win, and θ_E, precipitation, convergence and soil moisture all fall, as the maximum precipitation and convergence shifts from the Madeira basin to the nort hern Amazon basin of the river Negro as the sun moves northward.

Figure 5 shows the surface energy flux partition, plotted against the root zone SMI. R_{net}, latent heat flux, λE, and sensible heat flux, H, are all scaled by the clear sky flux, SW:SRF(clear), which removes the dependence on the solar zenith angle. Evaporative fraction, EF, defined as $\lambda E/(\lambda E+H)$, increases with SMI, while scaled λE itself varies very little with SMI. Here we are seeing the full impact of the coupling of the cloud and radiation fields on the surface energy budget. The increase of SMI and the associated increase in the cloud field (Figure 1(c)) appears in the coupled system as a decrease of R_{net} and H, while λE is almost constant. We shall see similar relationships using daily data later (Figure 11c).

2.2. Daily mean data for the Madeira river basin

The next three figures show the coupling of processes averaged over the Madeira river basin on the daily timescale for the period 1990-2001. First we look at the near-surface processes which are closely coupled to soil moisture. Figure 6a shows a scatterplot of P_{LCL} and RH (with slight approximation) as a function of first layer soil moisture index, SMI:L1. We also show the mean and standard deviation of the data binned in 0.1 ranges of SMI:L1. Near-surface RH increases and the mean LCL of cloud-base falls as SMI increases on the daily timescale. The relationship using daily mean data is the same as in Figure 2. Note that this is a relationship between daily mean RH and SMI. There is also a similar relationship between the diurnal range of RH and LCL to SMI (not shown). Figure 6b, shows that the quasi-linear coupling of SMI with LCC, and LW_{net}, seen in Figures 1c and 1d on a monthly time-scale, can also be seen in these daily data. Schär et al. (1999) noted the importance of the LW feedback on the surface energy budget. Considering the wide range of synoptic and advective processes that may have existed over the 12-year period, the standard deviations of these daily data, even though averaged over a large river basin, seem surprisingly small.

Figure 7a shows that daily mean TCWV and ALB:SRF are linked, with some scatter, to the mid-tropospheric mean daily omega field, Ω_{mid}. For $\Omega_{mid} = 0$ (vertical dashes), ALB:SRF≈0.31and TCWV≈41 kg m^{-2}. As expected, ALB:SRF and TCWV increase with mean ascent ($\Omega_{mid} < 0$), as the atmosphere moves towards saturation, and decrease with mean subsidence. This means that cloud albedo and precipitable water are closely related. Figure 7b shows that the dependence of ALB:SRF (right-hand-scale) on TCWV is weakly non-linear. Precipitation P also increases with TCWV, but the scatter is relatively larger, and the relationship is more non-linear.

Figure 8a shows that precipitation has a quasi-linear dependence on Ω_{mid}, and P goes to zero with mean subsidence $\Omega_{mid} \approx 40$ hPa day^{-1}, while evaporation is largely independent of the mid-tropospheric dynamics. Broadly speaking, P > E for mean ascent and P < E for mean descent, although for $\Omega_{mid} = 0$, in the mean P exceeds mean E by more than 1 mm day^{-1} for this basin, as runoff is a significant component of the water budget. 40 hPa day^{-1} is a characteristic mean radiatively driven subsidence in the subsiding branch of the tropical circulation (Betts and Ridgway, 1988, 1989), so we have fitted a regression line through $\Omega_{mid} = 40$ hPa day^{-1} for illustration. This suggests that we can think of (Ω_{mid} - 40) as a measure of the convective mass circulation that is linked to precipitation. Figure 7b showed that P also increases with TCWV. Figure 8b shows the near-linear relationship that we get for precipitation, if we combine TCWV with an estimate of the lower tropospheric convergence into convective systems (Ω_{mid} -40)/420. (The 420hPa numerator was adjusted to give the1-to-1 line fit.) Figures 7 and 8 are very useful. They show the link on the daily timescale between precipitation, the cloud field albedo, precipitable water and the large-scale dynamics that Figure 3 showed on the monthly timescale. It is only because we are sampling the omega field on the hourly timescale (which is adequate to resolve the rather large diurnal cycle (Betts and Jakob, 2002b)) that we get such satisfactory relationships.

Section 2.2 has shown that the daily-mean land-surface and atmospheric state (here derived from river-basin means) can be used to map the state transitions of the ‘climate’ of a model; and to quantify the links between the soil moisture, the cloud field (including mean cloud-base and cloud albedo), the short-wave (SW) and

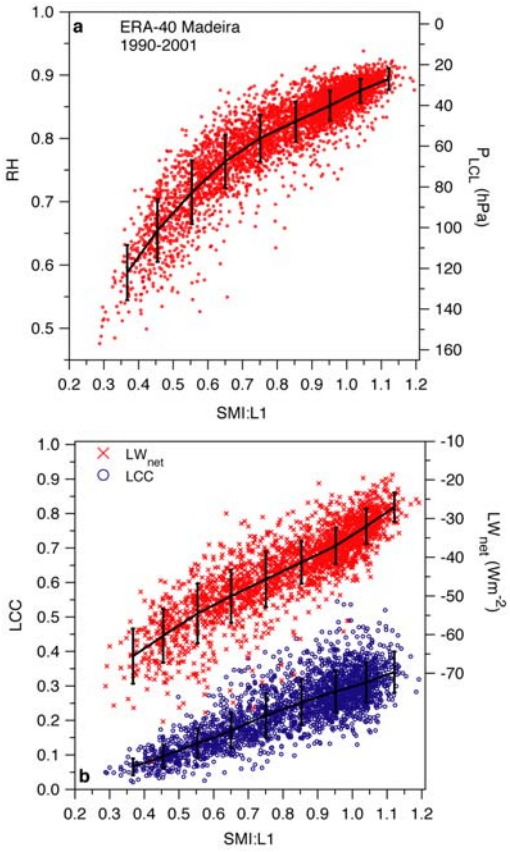

Figure 6: Scatterplot of daily means (1990-2001) of (a) P_{LCL} and RH as a function of soil moisture index (b) LCC and LW_{net} as a function of soil moisture index.

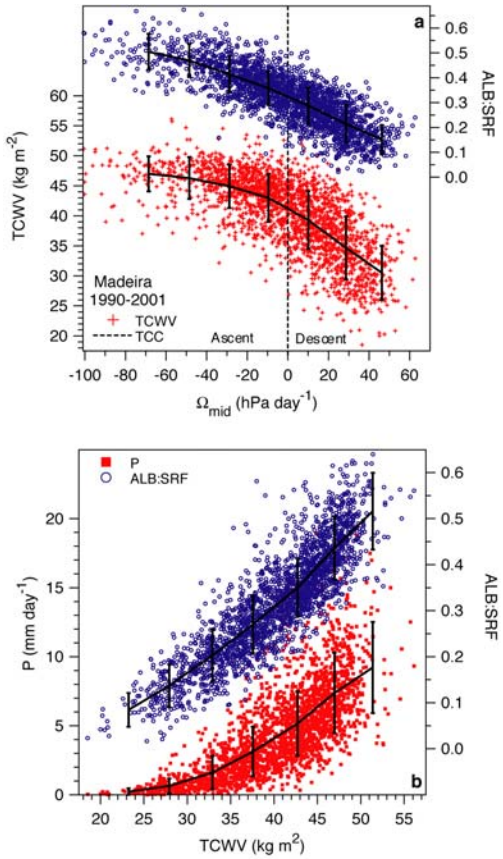

Figure 7(a) TCWV and ALB:SRF as a function of mid-tropospheric, Ω_{mid} and (b) P and ALB:SRF as a function of TCWV.

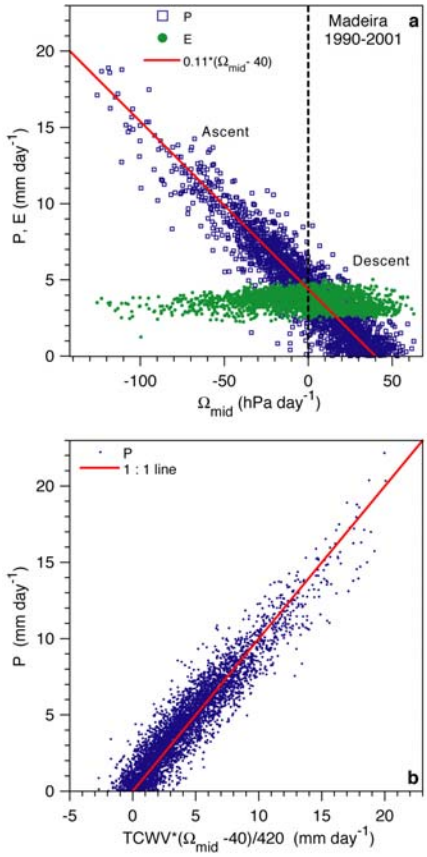

Figure 8(a) P and E as a function of mid-tropospheric, Ω_{mid} and (b) P plotted against an estimate of precipitation.

long-wave (LW) radiation fields at the surface, the vertical motion field, the atmospheric precipitable water and the surface precipitation. This gives us a powerful methodology for understand the feedback and coupling between different physical processes in the model, including the critical cloud radiative feedbacks. It also gives us a framework for comparing different models with each other and with data.

3. Cloud forcing terms in the radiative budget

Section 2.2 showed some of the surface and dynamic processes linked to the cloud field. In this section we present, again using daily mean data, the cloud-radiation relationships defined in equations (1), (2) and (3).

3.1. Relationship of surface and atmospheric cloud forcing to TOA forcing

Figure 9(a) shows the very tight relationship between the surface (left-hand axis) and TOA SW cloud forcing. The difference of these, the atmospheric cloud forcing SWCF:ATM (on the expanded right-hand axis), shows that the increased atmospheric absorption by the cloud field is only a small fraction of the TOA reflection. In ERA-40, the relationship between the SWCF:TOA and SWCF:SRF is very tight, and essentially identical across different Amazon sub-basins (not shown). The lower panel (9b) is a corresponding plot for the LW cloud forcing. Increasing cloud cover reduces the cooling to space and of the atmosphere, but has rather a small impact at the surface in this moist tropical atmosphere. The distributions for other Amazon sub-basins are again rather similar (not shown).

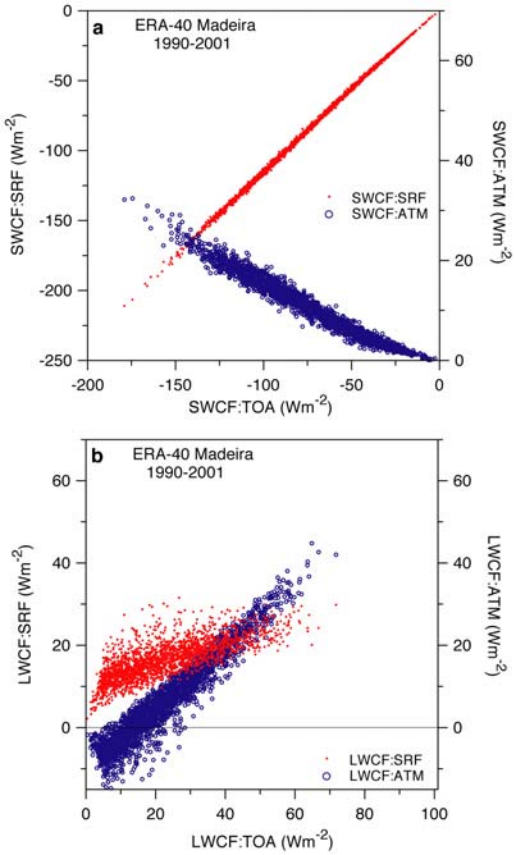

Figure 9(a) Surface and atmospheric SW cloud forcing as a function of TOA SW cloud forcing for Madeira River, (b) as (a) for LW cloud forcing.

3.2. SW and LW coupling to the cloud field

The TOA cloud albedo can be used as a rather precise surrogate for cloud amount for all the SW fluxes. We saw an indication of this in Figure 3(a) on the seasonal timescale. Using the daily mean data, we binned the

radiative fluxes in 0.02 ranges of ALB:TOA, giving Figure 10 for the mean and standard deviation of some key components of the radiation budget. Figure (10a) shows SW fluxes scaled by the TOA clear sky net flux, SW:TOA(clear), and in addition the surface cloud albedo, ALB:SRF (which is scaled by SW:SRF (clear). The upper (light-solid) curve for scaled SW:TOA is just (1-ALB:TOA). The scaled SW absorption in the atmosphere (heavy dashes) and SWCF:ATM (dotted) both increase weakly with cloud amount. The clear sky absorption is almost a constant fraction 0.255 of the SW:TOA(clear) for this basin (not shown). The scaled surface SW flux (heavy solid) is just the difference of scaled SW:TOA and the SW absorption. All the standard deviations are remarkably small, considering we have 12 years of daily model data. The daily scaled atmospheric and surface SW components are determined to better than 1% by the ALB:TOA, and their dependence is closely linear. Finally we show (light-dash) the surface cloud albedo, which has a very weak quadratic dependence on the TOA albedo, given (to better than 0.004) by

$$\text{ALB:SRF} = 1.45*\text{ALB:TOA} + 0.35*(\text{ALB:TOA})^2 \qquad (5)$$

The lower panel shows the unscaled LW fluxes as functions of ALB:TOA. At the surface the daily LW_{net} and its cloud forcing component, LWCF:SRF, are determined by the ALB:TOA with rather small standard deviation (about 8% of LW_{net}), even though the cloud albedo is a daytime parameter. For the atmosphere however the variance is much larger, and in fact the mean distribution differs for the different cloud distributions in the dry and rainy seasons (not shown).

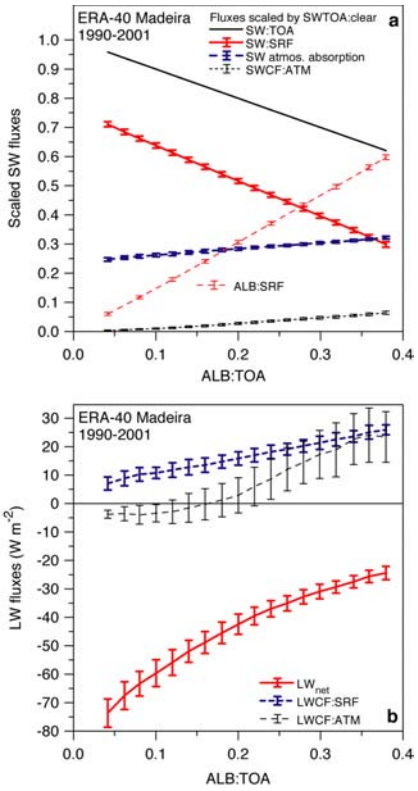

Figure 10(a) Scaled SW fluxes and ALB:SRF, and (b) surface LW_{net} and LW cloud forcing, as functions of ALB:TOA.

4. Coupling of cloud and surface processes

4.1. Stratification by cloud albedo and soil moisture

Figure 11 contrasts the stratification of the data by ALB:SRF (upper panels) and soil moisture index (lower panels). Panel (11a) is the surface energy budget, scaled by SW:SRF(clear), as a function of ALB:SRF. In the scaled budget, recall that the terms are still related as follows:

$$R_{net} = SW_{net} - LW_{net} \approx \lambda E + H \quad (6)$$

In Figure 11, we have reversed the sign of LW_{net}. Both outgoing LW_{net} and incoming SW_{net} increase with decreasing cloud albedo, so that the increase of R_{net} is reduced. The sensible heat flux also increases almost linearly with SW_{net}, so that the latent heat, which balances the surface energy budget, is essentially flat for low cloud albedos, and declines as cloud reflectance increases. The surface EF increases with increasing cloud albedo. SW_{net}, because it is simply (1-ALB:SRF) has no error bars on panel (a). The stratification by soil moisture (panel (11c)) has many similarities (notice also the similarities to the seasonal Figure 5), although there are larger standard deviations on R_{net} and SW_{net}, since this was not the basis for stratification. The latent heat flux, λE, has a weak maximum at SMI:L1 = 0.8. Both panels (11a) and (11c) show the similar roles of LW_{net} and H in the surface energy budget.

On the right is the link between the precipitation and mid-tropospheric omega and ALB:SRF (panel (11b)) and SMI:L1 (panel (11d)). As expected, more reflective cloud and moister soils are associated with greater precipitation and stronger mean ascent. Note that the standard deviations are smaller for the cloud albedo stratification than for soil moisture, and the mean relationships are more 'linear'. The cloud albedo is a better indicator of the large-scale ascent which links P and Ω_{mid} (Figure 8a). We have also added a stratification of P into three ranges of low level θ_E (θ_E <345K; 345<θ_E <351; θ_E >351K). We see as expected that P increases with θ_E as well as with soil moisture and albedo, but the effect is much smaller with the ALB stratification than the SMI stratification, which is more closely linked to surface RH. The standard deviations for this θ_E stratification are not significantly reduced (not shown).

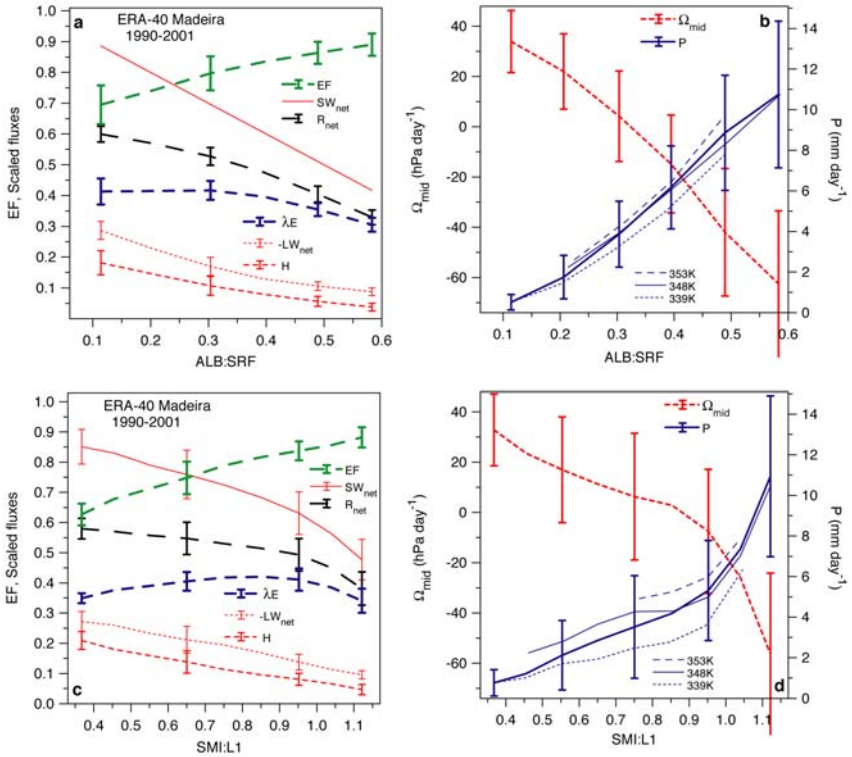

Figure 11: EF and scaled surface fluxes stratified by surface cloud albedo (a) and soil moisture index (c). Mid-tropospheric omega and daily precipitation stratified by surface cloud albedo (b) and soil moisture index (d). Precipitation is further stratified by θ_E, with the mean values of the ranges shown.

4.2. Dependence of RH and θ_E on soil moisture, precipitation and temperature

Figure 6a showed a scatterplot of RH and P_{LCL} on SMI. Figure 12a shows that some of the scatter is associated with precipitation. We have stratified the data into 0.1 bins of SMI:L1 and four ranges of P (in mm day^{-1}), showing only a representative set of standard deviations. Now we see that RH increases and P_{LCL}

decreases both with increasing SMI and with increasing P. The underlying link here is probably that the evaporation of precipitation in the sub-cloud layer increases RH and lowers the LCL. Significantly, Figure12a is not a function of temperature. This is a coupled system however. The curve for P<1 represents closely the direct link between soil moisture, resistance to evaporation and relative humidity. In the presence of significant precipitation, both RH (and P_{LCL}) and SMI:L1 (but not the root-zone SMI) respond on the daily time-scale. Indeed the first soil layer was given a 7-cm thickness to give a good response to precipitation on this timescale (Viterbo and Beljaars, 1995).

Figure 12b shows that mean θ_E increases both with soil moisture and with temperature (in 1K bins). The dependence on soil moisture is easy to understand as coming directly from the dependence of RH on SMI, essentially a local surface-BL coupling. The additional dependence of RH on P, seen in Figure 12a, accounts for about half the variance in each temperature range (not shown). However the dependence of θ_E on temperature is as large as the dependence on SMI (both have a range of 10-15K), and the temperature equilibrium is much more complex. It involves a surface energy balance dominated by evaporation, where R_{net} is influenced by the solar zenith angle and the cloud field, and an atmospheric temperature structure in which moisture convergence and latent heating as well as the radiation fields play important roles. This means that the increase of θ_E with soil moisture through RH can be clearly seen only if the temperature dependence is filtered as in Figure 12b (see Betts and Ball, 1998). The corresponding plot of daily maximum θ_E is similar to Figure 12b, with an upward shift of 4-5K (not shown).

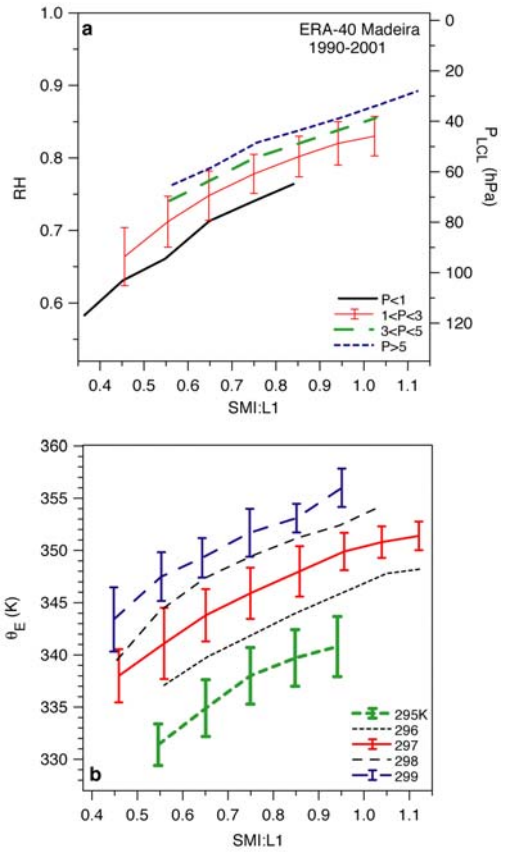

Figure 12(a) Dependence of RH and P_{LCL} on soil moisture index and precipitation and (b) Dependence of θ_E on soil moisture index and temperature.

4.3. Stratification by mean cloud-base, P_{LCL}

Soil moisture is not as readily observable as mean cloud-base P_{LCL}, which can be easily calculated from low level RH (it is very weakly dependent on temperature), or directly measured as the LCL of cloud-base by vertically pointing lidar (at least during the daytime in moist environments such as Amazonia). So we also

stratify the data into 20 hPa ranges of P_{LCL}. Figure 13a summarizes the mean variation with P_{LCL} of the surface cloud albedo, and SMI:L1 on the left-hand-scale, and mean precipitation on the right-hand-scale. All the variables shown decrease non-linearly as the sub-cloud layer deepens; precipitation has the most non-linear behavior and not surprisingly the largest variance. Figure 13b remaps into the P_{LCL} framework EF and the surface energy balance terms (from (6)). The energy balance is largely a remapping of Figure 11 (c), because of the link between SMI and P_{LCL} shown in Figure 12. The quasi-linear decrease of EF and increase of H with P_{LCL}, are consistent with the idealized model of Betts et al (2004). H increases with P_{LCL} because the surface sensible heat flux largely balances the diabatic processes, such as radiation and the evaporation of falling precipitation, which cool the subcloud layer, because the sensible heat flux at cloud base is only a small fraction of the surface flux (Betts, 1973). The result of this H dependence, given the SW and LW cloud feedbacks that control the weak variation of R_{net} with P_{LCL}, is again that λE has little variation with P_{LCL} and surface RH.

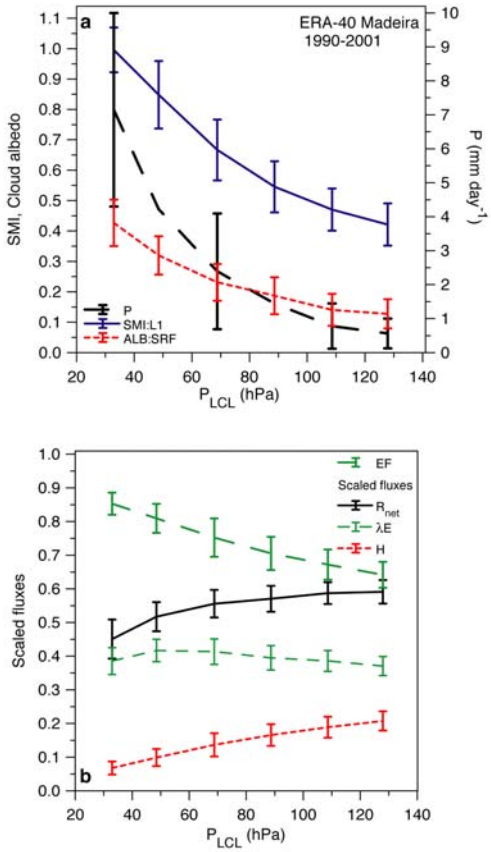

Figure 13: (a) Dependence of surface cloud albedo, SMI:L1 and precipitation on P_{LCL} (b) Dependence of EF and scaled surface fluxes on P_{LCL}.

Figure 14a shows surface LW_{net} as a function of P_{LCL}, also stratified by the ALB:SRF. Lower LCL is systematically associated with more cloud reflectance, and higher LCL with more outgoing LW_{net}. Given cloud-base (or surface RH) and this shortwave measure of the cloud field, the net surface LW is known to ±3 to 4Wm^{-2}, quite a remarkable precision. Figure 14b rearranges the data (for the same P_{LCL} stratification) to show the quasi-linear increase of LW_{net} and the non-linear increase of surface cloud albedo as a function of the surface EF. This is one link by which the surface evaporation feeds back on the surface energy budget through the LW and SW radiation fields. These are large effects. The SW cloud albedo range of 0.35 is comparable to the difference in albedo between vegetated and desert land surfaces, so clearly its tight coupling to the surface soil moisture (through cloud-base) and evaporation plays a central role in climate equilibrium over land. The mean value of SW:SRF (clear) is 260 W m^{-2} (annual range 200-295), so the SW cloud forcing range is of order 90 W m^{-2} , which is almost double the range of the LW cloud forcing. In the

moist tropics, the surface SW cloud forcing is the dominant term, so with an increased cloud field, the surface R_{net} is reduced (Figure 13b). The surface evaporation is just one component of the fully coupled system. Although the low level cloud field and RH are coupled to soil moisture and surface evaporation, the upper level clouds are largely a response to mean ascent (itself coupled to the release of latent heat from precipitation) and the convergence of moisture on the basin scale (Figures 7 and 8). At the same time, convective instability and precipitation requires high BL θ_E, which also comes from the surface interaction.

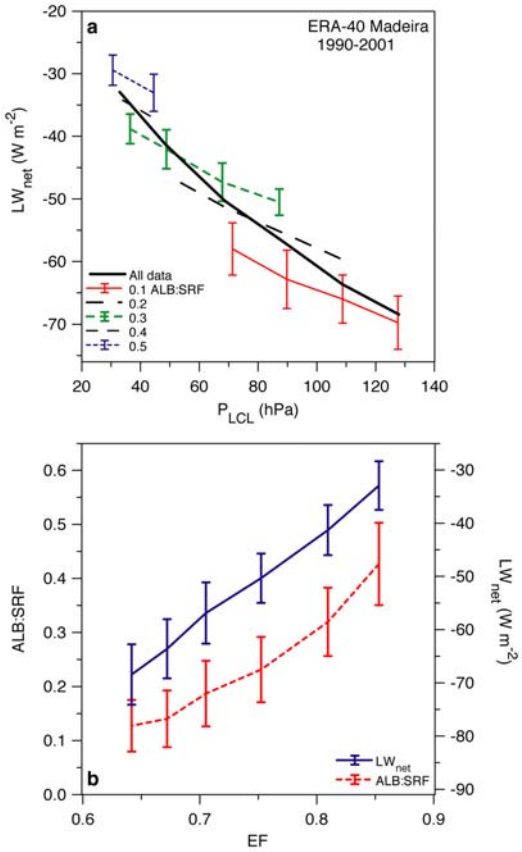

Figure 14(a) Dependence of LWnet on P_{LCL} and surface cloud albedo (b) Dependence of surface cloud albedo and LW_{net} on EF.

5. Conclusions

Models are a powerful tool for understanding the coupling of physical processes. We chose the Madeira river, a south-western basin of the Amazon, for illustration because it has a large seasonal cycle with a dry season in the austral winter. The mean seasonal cycle shows that surface RH and mean LCL, low cloud cover and LW_{net} are linked closely to soil moisture, while upper level cloud, precipitable water and precipitation are more closely linked to moisture convergence and mean ascent. The annual cycle of the surface radiative forcing depends not only on the changing solar zenith angle, but heavily on the cloud radiative forcing at the surface, in which the SW forcing dominates over the opposing LW cloud forcing. In fact surface R_{net} peaks in October, two months before solar zenith. However the rainy season is maintained till March, three months after solar zenith because the excess of precipitation over evaporation maintains high soil moisture, and high RH, which maintains θ_E for several months in the face of lower R_{net}.

We then showed that most of the links seen on the seasonal timescale can also be seen in daily averaged data, derived from basin-averaged hourly data. In fact, the daily-mean land-surface and atmospheric state can be used to map the state transitions of the 'climate' of a model; and to quantify the links between the soil moisture, the cloud field (including mean cloud-base and cloud albedo), and the short-wave (SW) and long-wave (LW) radiation fields at the surface, the vertical motion field, the atmospheric precipitable water and

the surface precipitation. This gives a powerful description of the coupling of physical processes in the model over land. Several important near-surface processes are strongly coupled to the first layer soil moisture: RH which gives LCL and the mean mixed layer depth, low cloud cover and the surface LW_{net}. In contrast, column water vapor, the albedo of the total cloud field and precipitation are linked more closely to the large-scale dynamics, represented here by the mean mid-tropospheric omega field. The SW cloud forcing of the atmosphere is given by the TOA cloud field albedo to better than 1% and the surface cloud albedo can be computed from the TOA cloud albedo to better than 0.5%. The surface outgoing LW_{net} decreases with RH (and therefore soil moisture) as well as with cloud cover, and this plays an important role in the surface radiation balance, reducing the impact of the SW cloud forcing.

Surface evaporation is controlled as much by the feedback of the cloud field on the surface radiation budget as by soil moisture. In fact, the sensible heat flux decreases with increasing cloud cover and soil moisture, while evaporation is relatively flat. The cloud albedo, because of its link to mean ascent, is a useful indicator of both precipitation and mid-tropospheric omega in the model. Surface RH (which is closely related to LCL, essentially a measure of mean cloud-base in the moist tropics) increases with first layer soil moisture, with a secondary increase with precipitation, probably associated with the evaporation of precipitation into the BL. Significantly these relations are independent of temperature. Consequently the link between BL θ_E and SMI can be clearly seen once the temperature dependence is filtered, as suggested earlier by Betts and Ball (1998). The surface RH (and the LCL) is an important link between several processes, and could be a useful parameter for stratification in comparisons with data, because RH is more easily observed than soil moisture. This we leave for later work.

We show that both LW_{net} and surface cloud albedo increase with the surface EF. This is one link by which the surface evaporation feeds back on the surface energy budget through the LW and SW radiation fields, and it is a large effect. The SW cloud albedo range with EF of 0.35 is comparable to the difference in albedo between vegetated and desert land surfaces, so its coupling to the surface soil moisture and evaporation plays a central role in climate equilibrium over land.

We have developed a powerful methodology to describe and understand the coupling and feedbacks between different physical processes in the model, including soil moisture, the BL equilibrium on the daily timescale, the vertical motion field and the critical cloud radiative feedbacks. This also gives us a framework for comparing different models with each other and with data. ERA-40 has already been compared over land on monthly time-scales with standard meteorological data, such as 2-m temperature and precipitation, and we know the biases are relatively small in recent decades (e.g. Betts et al. 2003a,b, 2005b). However, the relationships we present here have for the most part not been carefully evaluated, and some of course are hard to evaluate on the scale of a river basin. Our next task will be to intercompare model and data at points where detailed flux tower measurements exist for the components of the surface water and energy budgets. We shall also repeat this work with the next reanalysis, since recent changes to the convection code (Bechtold et al., 2004) have improved the diurnal cycle of precipitation over land in the tropics, which may have affected the coupling between clouds and surface processes.

Acknowledgments. Alan Betts acknowledges support from NASA under Grant NAS5-11578 and from NSF under Grant ATM-9988618, and from ECMWF for travel. It is a pleasure to acknowledge the entire ERA-40 team for their assistance.

References

Bechtold, P., J.-P. Chaboureau, A. Beljaars, A. K. Betts , M. Miller, M. Köhler, M. Miller and J.-L. Redelsperger, 2004: The simulation of the diurnal cycle of convective precipitation over land in a global model. *Q. J. R. Meteorol. Soc*., In press.

Betts, A. K., 1973: Non-Precipitating Convection and Its Parameterization. *Quart. J. Roy. Meteor. Soc.*, **99**, 178-196.

Betts, A. K. and W. Ridgway, 1988 : Coupling of the radiative, convective and surface fluxes over the equatorial Pacific. *J. Atmos. Sci.*, **45**, 522-536.

Betts, A.K. and W. L. Ridgway, 1989: Climatic equilibrium of the atmospheric convective boundary layer over a tropical ocean. *J. Atmos. Sci.*, **46**, 2621-2641.

Betts, A.K. and J.H. Ball, 1995: The FIFE surface diurnal cycle climate. *J. Geophys. Res.* **100**, 25679-25693.

Betts A. K. and J. H. Ball, 1998: FIFE surface climate and site-average dataset:1987-1989. *J. Atmos Sci* , **55,** 1091-1108.

Betts, A. K., J.H. Ball, A.C.M. Beljaars, M.J. Miller and P. Viterbo, 1996: The land-surface-atmosphere interaction: a review based on observational and global modeling perspectives. *J. Geophys. Res.* **101**, 7209-7225.

Betts, A. K., M. L. Goulden, and S.C. Wofsy, 1999: Controls on evaporation in a boreal spruce forest. *J. Climate*, **12**, 1601-1618.

Betts, A. K. and C. Jakob, 2002a, Evaluation of the diurnal cycle of precipitation, surface thermodynamics and surface fluxes in the ECMWF model using LBA data.. *J. Geophys. Res.*, **107**, 8045, doi:10.1029/2001JD000427.

Betts, A. K. and C. Jakob, 2002b, Study of diurnal cycle of convective precipitation over Amazonia using a single column model. *J. Geophys. Res.*, **107**, 4732, doi:10.1029/2002JD002264.

Betts, A.K., 2003: The diurnal cycle over land. Chapter 6, pp. 73-93, of *"Forests at the Land-Atmosphere interface"* ISBN: 0-85199-677-9, 304pp, Eds., M Mencuccini, J Grace, J Moncrieff and K. McNaughton, publisher CABI Publishing, Wallingford, Oxon OX10 8DE, UK.

Betts, A. K., J. H. Ball, M, Bosilovich, P. Viterbo, Y.-C. Zhang, and W. B. Rossow, 2003a: Intercomparison of Water and Energy Budgets for five Mississippi Sub-basins between ECMWF Reanalysis (ERA-40) and NASA-DAO fvGCM for 1990-1999. *J. Geophys. Res.*, **108** (D16), 8618, doi:10.1029/2002JD003127.

Betts, A. K., J. H. Ball and P. Viterbo, 2003b: Evaluation of the ERA-40 surface water budget and surface temperature for the Mackenzie River basin. *J. Hydrometeorology*, **4**, 1194-1211.

Betts, A. K., 2004: Understanding Hydrometeorology using global models. *Bull. Amer. Meteorol. Soc.*, **85**, 1673-1688.

Betts, A. K., B. Helliker and J. Berry, 2004, Coupling between CO_2, water vapor, temperature and radon and their fluxes in an idealized equilibrium boundary layer over land. *J. Geophys. Res.*, 109, D18103, doi:10.1029/2003JD004420.

Betts, A. K., R. Desjardins and D. Worth, 2005a: Impact of agriculture, forest and cloud feedback on the surface energy balance in BOREAS. [for publication in *Agric. Forest Meteorol*. special issue].
ftp://members.aol.com/akbetts/AgricForest_Bettsetal.pdf

Betts, A. K, J.H., Ball, P. Viterbo, A. Dai and J. A. Marengo, 2005b: Hydrometeorology of the Amazon in ERA-40. [submitted to *J. Hydrometeorology*]

Findell, K.L. and E.A.B. Eltahir, 2003. Atmospheric controls on soil moisture-boundary layer interactions. Part I: Framework development. *J. Hydrometeorology*, **4**, 552-569.

Kållberg, P., A., Simmons, S., Uppala and M. Fuentes, 2004: The ERA-40 archive. *ERA-40 Project Report*, No. **17**. ECMWF, Shinfield Park, Reading RG2 9AX, UK., 31pp.

Koster, R. D., P. A. Dirmeyer, A. N. Hahmann, R. Ijpelaar, L. Tyahla, P. Cox, and M. J. Suarez: Comparing the Degree of Land-Atmosphere Interaction in Four Atmospheric General Circulation Models, 2002: *J. Hydrometeorology*, **3**, 363-375.

Koster, R. D., P. A. Dirmeyer, Z. Guo and the GLACE team, 2004: Regions of anomalously strong coupling between soil moisture and precipitation. *Science*, **305**, 1138-1140.

Lawrence, D.M. and J.M. Slingo, 2004: Weak land-atmosphere coupling strength in HadAM3: the role of soil moisture variability. Submitted to *J. Hydrometeorology*.

Pinker, R. T and 13 co-authors, 2003: Surface radiation budgets in support of the GEWEX Continental-Scale International Project (GCIP) and the GEWEX Americas Prediction Project (GAPP), including the North American Land Data Assimilation System (NLDAS) project. *J. Geophys. Res.*, **108** (D22), doi:10.1029/2002JD003301.

Schär, C., D. Lüthi, U. Beyerle and E. Heise, 1999: The soil-precipitation feedback: a process study with a regional climate model. *J. Climate*, **12**, 722-741.

Small, E. E. and S. A. Kurc, 2003: Tight coupling between soil moisture and the surface radiation budget in semiarid environments: Implications for land-atmosphere interactions. *Water Resources Res.*, **39**, 10, 1278, doi:10.1029/2002WR001297.

Uppala, S.M., P.W. Kållberg, A.J. Simmons, U. Andrae, V. da Costa Bechtold, M. Fiorino, J.K Gibson, J. Haseler, A. Hernandez, G.A. Kelly, X. Li, K. Onogi, S. Saarinen, N. Sokka, R.P. Allan, E. Andersson, K. Arpe, M.A. Balmaseda, A.C.M. Beljaars, L. van de Berg, J. Bidlot, N. Bormann, S. Caires, F. Chevallier, A. Dethof, M. Dragosavac, M. Fisher, M. Fuentes, S. Hagemann, E. Hólm, B.J. Hoskins, L. Isaksen, P.A.E.M. Janssen, R. Jenne, A.P. McNally, J.-F. Mahfouf, J.- J. Morcrette, N.A Rayner, R.W. Saunders, P. Simon, A. Sterl, K.E. Trenberth, A. Untch, D. Vasiljevic, P. Viterbo and J. Woollen 2005: The ERA-40 Reanalysis. Submitted to *Quart. J. Roy. Meteorol. Soc*.

USGCRP, 1995, Our Changing Planet: The FY 1995 U.S. Global Change Research Program. Available at http://www.gcrio.org/OCP/toc.html.

Van den Hurk, B.J.J.M., P. Viterbo, A.C.M. Beljaars and A. K. Betts, 2000: Offline validation of the ERA40 surface scheme. *ECMWF Tech Memo, 295*, 43 pp., Eur. Cent. For Medium-Range Weather Forecasts, Shinfield Park, Reading RG2 9AX, England, UK.

Viterbo, P. and A.C.M. Beljaars, 1995. An improved land-surface parameterization in the ECMWF model and its validation. *J. Clim.*, **8**, 2716-2748.